

LETTER TO THE EDITOR

Cold dust around nearby stars (DUNES). First results[★]**A resolved exo-Kuiper belt around the solar-like star ζ^2 Ret**

C. Eiroa¹, D. Fedele^{1,2,3}, J. Maldonado¹, B.M. González-García⁴, J. Rodmann⁵, A. M. Heras⁶, G.L. Pilbratt⁶, J.-Ch. Augereau⁷, A. Mora^{8,1}, B. Montesinos⁹, D. Ardila¹⁰, G. Bryden¹¹, R. Liseau¹², K. Stapelfeldt¹¹, R. Launhardt², E. Solano⁹, A. Bayo¹³, O. Absil¹⁴, M. Arévalo⁹, D. Barrado⁹, C. Beichmann¹⁵, W. Danchi¹⁶, C. del Burgo¹⁷, S. Ertel³¹, M. Fridlund⁶, M. Fukagawa¹⁸, R. Gutiérrez⁹, E. Grün¹⁹, I. Kamp²⁰, A. Krivov²¹, J. Lebreton⁷, T. Löhne²¹, R. Lorente²², J. Marshall²³, R. Martínez-Arnáiz²⁴, G. Meeus¹, D. Montes²⁴, A. Morbidelli²⁵, S. Müller²¹, H. Mutschke²¹, T. Nakagawa²⁶, G. Olofsson²⁷, I. Ribas²⁸, A. Roberge¹⁶, J. Sanz-Forcada⁹, P. Thébault²⁹, H. Walker³⁰, G. J. White^{23,30}, and S. Wolf³¹

(Affiliations can be found after the references)

Accepted May 11, 2010

ABSTRACT

We present the first far-IR observations of the solar-type stars δ Pav, HR 8501, 51 Peg and ζ^2 Ret, taken within the context of the DUNES *Herschel* Open Time Key Programme (OTKP). This project uses the PACS and SPIRE instruments with the objective of studying infrared excesses due to exo-Kuiper belts around nearby solar-type stars. The observed 100 μm fluxes from δ Pav, HR 8501, and 51 Peg agree with the predicted photospheric fluxes, excluding debris disks brighter than $L_{\text{dust}}/L_{\star} \sim 5 \times 10^{-7}$ (1 σ level) around those stars. A flattened, disk-like structure with a semi-major axis of ~ 100 AU in size is detected around ζ^2 Ret. The resolved structure suggests the presence of an eccentric dust ring, which we interpret as an exo-Kuiper belt with $L_{\text{dust}}/L_{\star} \approx 10^{-5}$.

Key words. Stars: general – Stars: planetary systems: planetary discs – Stars: planetary systems: formation - Space vehicles: instruments: *Herschel* Space Observatory, PACS

1. Introduction

The discovery of infrared excess emission produced by cold, optically thin disks composed of micron-sized dust grains around main sequence stars is one of the main contributions of IRAS (Aumann et al. 1984). Since the lifetime of such grains, set by destructive collisions, Poynting-Robertson drag and radiation pressure, is much shorter than the ages of these stars, one must conclude that those dust disks - called debris disks - are continuously replenished by collisions of large rocky bodies (Backman & Paresce 1993). Observations of debris disks provide powerful diagnostics from which to learn about the dust content, its properties and its spatial distribution; in addition, since dust sensitively responds to the gravity of planets, it can be used as a tracer of the presence of planets. Thus, observations of debris disks around stars of different masses and ages inform us about the formation and evolution of planetary systems, since they are a direct proof for the existence of planetesimals and an indirect tracer of the presence of planets around stars.

In the Solar System, the asteroid and Kuiper belts are examples of debris systems; in particular, the Kuiper belt has an estimated dust luminosity $L_{\text{dust}}/L_{\star} \sim 10^{-7}$ - 10^{-6} (Stern 1996). IRAS was only able to detect bright disks, $L_{\text{dust}}/L_{\star} > 10^{-4}$, mainly around A and F stars; ISO extended our knowledge to a wider spectral type range and found a general decline with the stellar age (Habing et al 2001, Decin et al. 2003). A remarkable step

forward has been achieved by *Spitzer*, studying debris disks as faint as $L_{\text{dust}}/L_{\star}$ several times 10^{-6} , their incidence from A to M type stars, the age distribution, the presence of planets, etc. (e.g. Su et al. 2006, Trilling et al. 2008, Bryden et al. 2009). *Spitzer* has, however, several limitations. Its poor spatial resolution prevent us from constraining fundamental disk parameters which require resolved imaging, and the confusion limit inherent in its large beam limits its detection capability to cold disks brighter than the Kuiper belt by around two orders of magnitude. Also, *Spitzer* is not sensitive longward of 70 μm , wavelengths particularly important for the cold disks generally found around Sun-like stars. The far-infrared 3.5 m diameter *Herschel* space telescope (Pilbratt et al. 2010) with its instruments PACS (Poglitsch et al. 2010) and SPIRE (Griffin et al. 2010) overcomes these limitations, offering the possibility of characterising cold, ~ 30 K, debris disks as faint as $L_{\text{dust}}/L_{\star}$ few times 10^{-7} with spatial resolution ~ 30 AU at 10 pc, i.e., true extra-solar Kuiper belts.

DUNES¹ is a *Herschel* OTKP designed to detect and characterize cold, faint, debris disks, i.e., extra-solar analogues to the Kuiper belt, around a statistically significant sample of main-sequence FGK nearby stars, taking advantage of the unique capabilities of *Herschel* with PACS and SPIRE. The data will be analysed with radiative, collisional and dynamical dust disk models. A complete description of DUNES goals, target selection, and stellar properties will be presented elsewhere (Eiroa et al. 2010, in preparation). The objectives of the DUNES survey are complementary to those of the OTKP DEBRIS (Matthews et

[★] Herschel is an ESA space observatory with science instruments provided by European-led Principal Investigator consortia and with important participation from NASA.

¹ *DUST* around *NEarby Stars*, <http://www.mpa-hd.mpg.de/DUNES/>.

Table 1. Summary of the SDP DUNES observations.

Star	Obs. ID	Mode ¹	Bands (μm)	Scan Direction	OT (sec)
q ¹ Eri	1342187139/40	SM	100/160	63°/117°	2536
q ¹ Eri	1342187141	PS	100/160		4714
q ¹ Eri	1342187142	PS	70/160		789
ζ^2 Ret	1342183660	PS	100/160		1572
ζ^2 Ret	1342191102/03	SM ²	100/160	117°/63°	4510
ζ^2 Ret	1342191104/05	SM ²	70/160	63°/17°	4510
δ Pav	1342187075/06	SM	100/160	45°/135°	3834
HR 8501	1342187145/46	SM	100/160	63°/117°	1890
51 Peg	1342187255	PS	100/160		1731

⁽¹⁾ SM = scan map; PS = chop-nod/point-source mode

⁽²⁾ Routine phase DUNES observing time (not SDP)

al. 2010). Both projects have complementary star samples, sharing partly some sources and the corresponding data.

The DUNES objectives require the detection of very faint excesses at the mJy level, comparable to the photospheric emission and only a few times the measurement uncertainties. The primary observing strategy is designed to integrate for as long as needed to detect the 100 μm photospheric flux, subject only to confusion noise limitations. In this letter we present our first results obtained during the science demonstration phase (SDP) of *Herschel*. Four solar-type G stars were observed: ζ^2 Ret, δ Pav, HR 8501, and 51 Peg. We also observed q¹ Eri as a test object with a well-known, bright debris disk; the q¹ Eri results are presented in an accompanying letter (Liseau et al. 2010). Excluding δ Pav, the rest of the stars are shared targets with DEBRIS.

2. Observations and data reduction

The stars were observed with PACS at 70 μm (blue), 100 μm (green), and 160 μm (red). Two observing modes were used - chop-nod/point-source (PS hereafter) and scan map (SM hereafter). Our data set allows us to make a direct comparison of both modes, specially in the cases of q¹ Eri and ζ^2 Ret. A critical evaluation of this comparison will be the subject of a technical note. SM observations of ζ^2 Ret were carried out as DUNES routine observations. Table 1 gives some details of the observations including the identification number, the observing mode, the wavelength bands, the scan direction angles, and the total duration of the observation (OT).

Data reduction was carried out using the *Herschel* Interactive Processing Environment (HIPE), version v2.0.0 RC3, and the pipeline script delivered at the December 2009 *Herschel* data reduction workshop, ESAC, Madrid, Spain. The script provides all the tools to convert pure raw PACS/*Herschel* data to flux calibrated and position rectified images. While the instrument pixel size is 3''.2 for the blue and green bands and 6''.4 for the red band, the resolution of the final images is set to 1''/pixel and 2''/pixel for the blue/green and red bands, respectively.

3. Results

3.1. δ Pav, HR 8501, 51 Peg

Table 2 gives J2000.0 equatorial coordinates of δ Pav, HR 8501 and 51 Peg at 100 μm , as well as their optical positions. PACS positions are corrected from the proper motions of the stars. Differences between the optical and 100 μm positions are within the uncertainties for *Herschel* pointing. Of the three stars, only δ Pav has been detected at 160 μm .

100 μm FWHM values of δ Pav have been estimated using a 2-D gaussian fit. This procedure did not produce reasonable results for HR 8501, perhaps due to the faintness of the star; in this case the FWHM has been estimated from intensity profiles along the R.A. and Dec. directions. For 51 Peg, observed in PS mode, the FWHM estimate is also based on some additional point-like sources visible in the PACS field. The 100 μm FWHM estimates are given in Table 2. The 160 μm 2-D gaussian fit for δ Pav gives FWHM = 11''.8 \times 9''.2, with conservative errors $\sim 1''$. These values and the elongated beam are consistent with the expected results for point sources (see the technical notes PICC-ME-TN-035/036 in <http://herschel.esac.esa.int/AOTsReleaseStatus.shtml>)

Aperture photometry has been used to estimate the flux of the stars. Table 2 gives fluxes and errors taking into account the correction factors indicated in the aforementioned technical notes. The sky noise was 2.5×10^{-5} Jy/pixel and 2.7×10^{-5} Jy/pixel for the 100 μm SM data of δ Pav and HR 8501, respectively. The sky noise is considerably higher in the PS-mode 51 Peg image ($\approx 4.3 \times 10^{-5}$ Jy/arcsec²) due to the very irregular background and presence of negative signals. The 160 μm sky noise was 4.9×10^{-5} Jy/pixel for the δ Pav data. The absolute calibration uncertainties are 10% in the blue and green bands and better than 20% in the red band.

3.2. ζ^2 Ret (HIP 15371)

Fig 1 shows the SM PACS images of ζ^2 Ret. An East-West oriented structure is seen at 70 and 100 μm . It consists of two point-like flux peaks embedded in a faint, extended emission, which displays a secondary diffuse maximum at its Western side. Both point-like peaks have similar brightness in the green band, but the Eastern point-like peak is much fainter in the blue band. The two point-like sources are unresolved in the lower-resolution 160 μm image; instead a single bright peak is observed at that position with a secondary maximum at the position of the 70/100 μm Western diffuse emission.

Table 3 gives positions at 70 and 100 μm of both point-like sources, and of the brightest 160 μm peak; the optical position of ζ^2 Ret is also given for comparison. The brightest 70 μm peak coincides with the optical position of the star within the *Herschel* pointing error; this result and the fact that its PACS 70 and 100 μm fluxes are similar to the expected ζ^2 Ret photospheric fluxes (see below) lead us to identify this point-like PACS object with the optical star. There is a small shift between the 70 and 100 μm positions of ζ^2 Ret, but we note that a similar shift is found for other field objects - a blue object very close to the ζ^2 Ret complex towards the South-West; and two red objects, one towards the Northwest and one towards the Northeast (see Fig. 1).

The middle panels of Fig. 1 show isocontour plots. The optical position of ζ^2 Ret is marked. 100 μm and 160 μm contours have been spatially shifted so that the peak positions of the mentioned field objects coincide in all three bands (those objects are not shown in the isocontour plots). The size of the whole structure changes with wavelength from $\approx 25'' \times 15''$ in the blue to $\approx 40'' \times 15''$ in the red band. East-West intensity profiles are shown in the bottom of Fig. 1, together with similar profiles of α Bootis. The blue and green intensity profiles show the point-like character of ζ^2 Ret, as well as of the faint peak at the East, called PS-E hereafter; the profile in the red band also shows point-like behaviour for the brightest 160 μm peak, ζ^2 Ret+PS-E in Fig. 1 and Table 3. The Western diffuse peak ("W" in Fig. 1) appears very prominent in the green and red profiles, while it is very faint compared to ζ^2 Ret in the blue profile. North-South profiles (not

Table 2. Equatorial coordinates, FWHM at 100 μm , observed fluxes with 1σ statistical errors (F_{PACS}), and predicted photospheric fluxes (F_{\star}). Absolute PACS uncertainties are $\sim 10\%$ and less than 20% for 100 and 160 μm , respectively. Flux units are mJy.

Star	Optical position (J2000)	PACS 100 μm position (J2000)	PACS 100 μm			PACS 160 μm		
			FWHM	F_{PACS}	F_{\star}	FWHM	F_{PACS}	F_{\star}
δ Pav	20:08:43.61 -66:10:55.4	20:08:43.53 -66:10:58.1	$6'3 \times 6'2$	59.6 ± 1.1	68.7	21.0 ± 1.5	26.9	
HR 8501	22:18:15.62 -53:37:37.5	22:18:16.14 -53:37:37.1	$6'3 \times 6'2$	9.8 ± 1.2	10.9			4.3
51 Peg	22:57:27.98 +20:46:07.8	22:57:28.44 +20:46:08.5	$5'9 \times 6'0$	11.3 ± 1.7	10.8			4.2

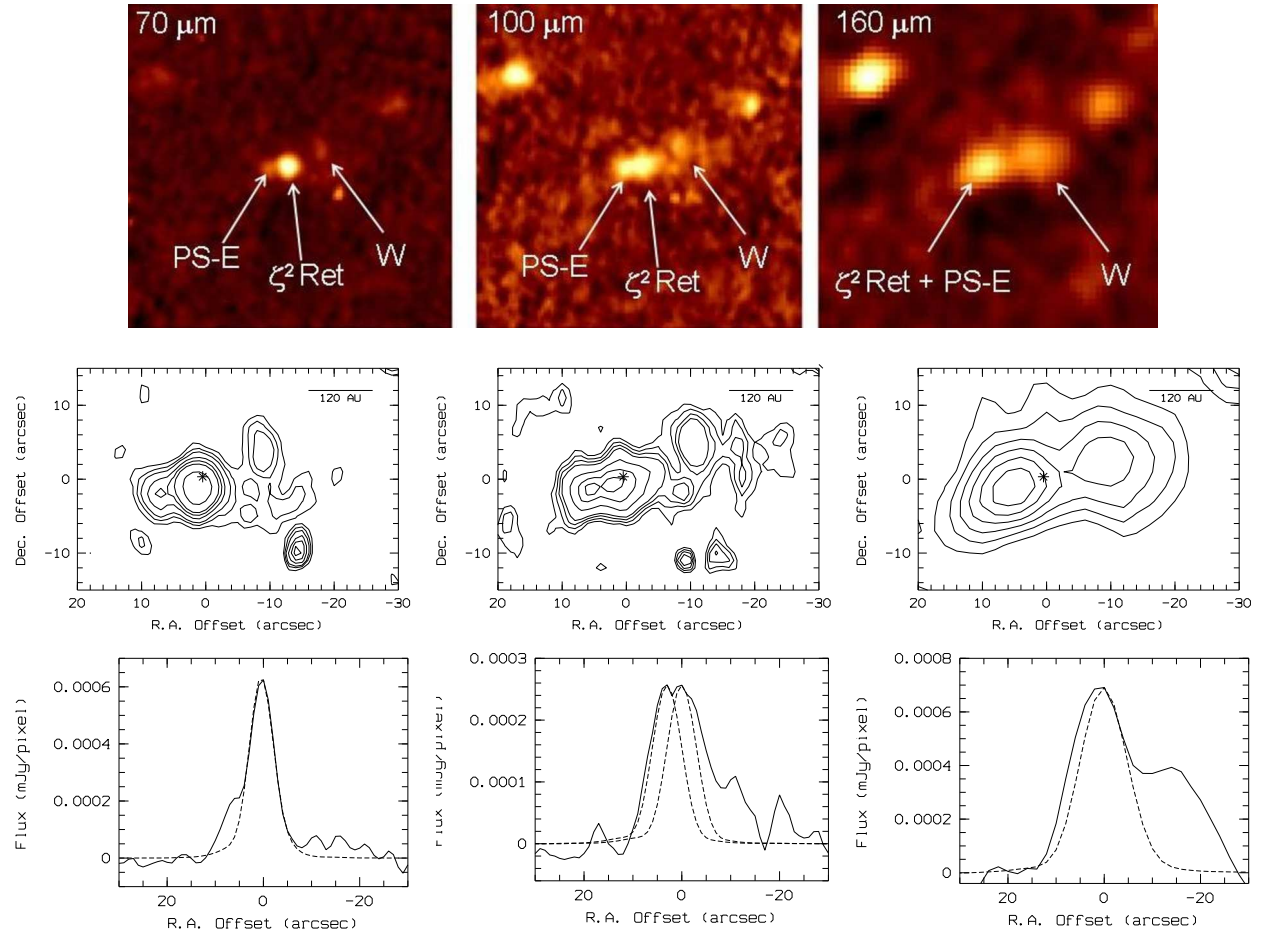


Fig. 1. PACS results of ζ^2 Ret. Panels from left to right: 70 μm , 100 μm , and 160 μm . Upper panel: Field size is $100'' \times 100''$ with East to the left and North up. Middle panels plot isocontours. Note that the field size is different from that displayed in the upper panels. The “star” symbol, position (0,0), corresponds to the optical star (Table 3). A segment indicating 120 AU is shown. Contours: 70 μm : 3,4,6,9,12,15,24 σ , 100 μm : 3,4,5,6,12,14 σ , 160 μm : 3,6,9,12,15,18 σ (1σ values are indicated in the text). Lower panels: R.A. intensity profiles through the peak flux of ζ^2 Ret (solid line). For comparison, R.A. intensity profiles of the calibration star α Bootis are also plotted (dashed lines), scaled to the peak flux of ζ^2 Ret (70 and 100 μm) and ζ^2 Ret+PS-E (160 μm). The α Bootis profile is also scaled and superimposed to PS-E in the 100 μm panel.

shown) do not resolved either ζ^2 Ret, PS-E, or ζ^2 Ret+PS-E in any band, i.e. they are point-like along that direction with no hint of any faint extended emission.

Table 3 gives PACS fluxes estimated using the flux peaks of the point-like sources and integrating over beam sizes given by π (FWHM_x \times FWHM_y) / 4 ln 2. The PACS source identified with ζ^2 Ret is a blue object, while PS-E is a red one. The flux at 160 μm corresponds to ζ^2 Ret+PS-E, but PS-E is the main contributor to the flux at this wavelength - the emission is peaking more towards PS-E (Fig. 1). The total flux of the ζ^2 Ret complex is 44.5 mJy, 40.4 mJy, and 42.6 mJy in the blue, green and red bands, respectively. The estimated 70 μm flux for the whole

complex agrees very well with the unresolved *Spitzer* flux of 46 mJy at the same wavelength (Trilling et al. 2008).

4. Discussion

Our data do not reveal any cold dust disk around δ Pav, HR 8501 or 51 Peg, since the observed and predicted 100 μm photospheric fluxes coincide within the uncertainties (Table 2). Assuming dust temperatures of 40 K (peak blackbody fluxes at $\sim 100 \mu\text{m}$), we can exclude debris disks with $L_{\text{dust}}/L_{\star} \gtrsim 5 \times 10^{-7}$ (1σ) (Eqn. 4 from Beichmann et al. 2006).

ζ^2 Ret, located at 12 pc, is a G1 V star with a bolometric luminosity of $0.97 L_{\odot}$ and an estimated age of $\sim 2\text{-}3$ Gyr (Eiroa

Table 3. Coordinates, fluxes, and 1σ statistical errors of the ζ^2 Ret PACS point-like sources. Flux units are mJy.

Object	α (2000.0)	δ (2000.0)	Flux
ζ^2 Ret (optical)	03:18:12.82	-62:30:22.9	
ζ^2 Ret (70 μ m)	03:18:12.77	-62:30:23.2	24.9 \pm 0.8
ζ^2 Ret (100 μ m)	03:18:13.12	-62:30:24.4	13.4 \pm 1.0
PS-E (70 μ m)	03:18:13.63	-62:30:24.2	8.9 \pm 0.8
PS-E (100 μ m)	03:18:13.55	-62:30:24.4	13.5 \pm 1.0
ζ^2 Ret+PS-E (160 μ m)	03:18:13.37	-62:30:23.2	19.4 \pm 1.5

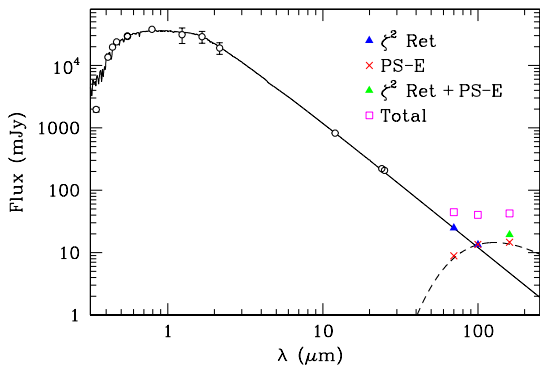


Fig. 2. SED of ζ^2 Ret. Optical, 2MASS, IRAS, and *Spitzer* fluxes are indicated by black symbols. Blue triangles are ζ^2 Ret; red crosses are PS-E; green triangle is ζ^2 Ret+PS-E; magenta squares are total fluxes from the ζ^2 Ret complex. Error bars are smaller than the size of the symbols. The solid line is the best χ^2 photospheric fit ($T_{eff} = 5850$ K, $\log g = 4.5$, and $[Fe/H] = -0.23$, which are mean values found using the DUNES discovery tool, <http://sdc.laeff.inta.es/dunes>). The dashed line is a 40 K black body normalized at the PS-E 100 μ m flux. The deduced 160 μ m flux from PS-E is also plotted with a red cross (see text).

et al. 2010, in prep.). Figure 2 shows the stellar SED as well as PACS fluxes from PS-E and the whole complex; a PHOENIX stellar photosphere (Brott & Hauschildt 2005) is also plotted. The agreement between the observed 70 and 100 μ m fluxes from the blue bright point-source and those predicted by the photospheric fit, 24.7 mJy and 12.1 mJy at 70 and 100 μ m, respectively, is excellent. This photometry and its positional alignment with the stellar position support our claim that the PACS blue point-like object is indeed ζ^2 Ret. On the other hand, the nature of the extended structure is intriguing. While coincidental alignments with background objects are common in IRAS all-sky images, the much higher resolution of *Herschel* makes such juxtapositions unlikely within a targeted survey. Based on *Spitzer* source counts of background galaxies at 70 μ m (Dole et al. 2004), we find that the probability of chance alignment with a ≥ 20 mJy source within 10'' is just 10^{-3} .

The source PS-E is a red object with a black body temperature $T(70-100 \mu\text{m}) \approx 40$ K. We have pointed out that both PS-E and ζ^2 Ret are not resolved at 160 μ m and that the flux peak at this wavelength is closer to PS-E. If we subtract from the measured 160 μ m flux the stellar flux predicted for ζ^2 Ret (4.7 mJy) and make the plausible assumption that the residual flux (14.7 mJy) originates in PS-E, this 160 μ m flux for PS-E is again consistent with a ~ 40 K blackbody (see Fig. 2). PS-E is clearly not stellar; we suggest that it is instead orbiting circumstellar dust. The contribution of the extended emission to the total flux

can be estimated subtracting the point-like sources from the total flux reported above. The residual flux mainly corresponds to the Western diffuse emission since the point-like sources are not resolved along the North-South direction. In this case, the remaining flux corresponds to black body temperatures in the range ~ 30 -40 K, and the total fractional luminosity from the entire structure surrounding ζ^2 is $L_{\text{dust}}/L_{\star} \approx 10^{-5}$.

We have the interesting scenario of a **G1** V star surrounded by optically-thin 30-40 K emission. This is the temperature range expected for black body dust grains orbiting at distances ~ 100 AU from the star. This is consistent with the projected linear distances from ζ^2 Ret to PS-E and to the Western diffuse emission of ~ 70 AU and ~ 120 AU, respectively. The red image suggests a flattened, disk-like structure with the star located asymmetrically along the major axis, while the blue and green images suggest it is ring-like given the flux cavity towards the West from the star. We interpret the structure in the PACS images as a dust ring surrounding ζ^2 Ret. We attribute the observed East-West asymmetry to a significant disk eccentricity - $e \approx 0.3$. Similarly, an offset is observed in the Fomalhaut debris disk with $e \approx 0.1$ (Stapelfeldt et al. 2004). Maintaining a stable eccentric ring requires an external driving force such as a shepharding planet (Wyatt et al. 1999) and in the case of Fomalhaut the predicted planet has been been directly imaged (Kalas et al. 2008). The disk asymmetry in the ζ^2 Ret system may likewise be the signature of an unseen planetary companion. While this is an exciting possibility, other forces might also produce disk asymmetry. For example, interaction with the ISM is probably responsible for the strong asymmetry observed around HD 61005, since its brightness offset is well aligned with the star's space motion (Hines et al. 2007). A more profound analysis and detailed modeling of ζ^2 Ret and the suggested Kuiper belt is deferred to a future paper.

5. Conclusions

Our results show the capability of *Herschel*/PACS to detect and resolve cold dust disks with a luminosity close to the solar Kuiper belt, which will allows us to deepen our understanding of planetary systems, in particular those associated with mature stars. Specifically, our data exclude the existence of cold debris disks with $L_{\text{dust}}/L_{\star} \gtrsim 5 \times 10^{-7}$ (1σ) around the solar-type stars δ Pav, HR 8501 and 51 Peg. On the other hand, the data show that ζ^2 Ret is a good example where cold disks around nearby stars, very much alike the solar Kuiper belt, can be resolved and studied in great detail with the *Herschel* space observatory.

References

- Aumann H.H. et al. 1984 ApJ 278, L23
- Backman, D.E., & Paresce, F. 1993, in Protostars and Planets III, ed. E.H. Levy & J.I. Lunine (Tucson: Univ. Arizona Press), 1253
- Beichmann et al. 2006, ApJ 652, 1674
- Brott, I. & Hauschildt, P.H. 2005, ESA SP-576, C. Turon, K.S. O'Flaherty, M.A.C. Perryman (eds), p.565
- Bryden et al. 2009, ApJ 705, 1226
- Dole, H., Le Floc'h, E., Pérez-González, P. G., et al. 2004, ApJS, 154, 87
- Decin, G., Dominik, C., Waters, L.B.F.M. & Waelkens, C. 2003, ApJ 598, 636
- Griffin et al. 2010, this volume
- Habing, H.J. et al. 2001, A&A 365, 545
- Hines, D. C., Schneider, G., Hollenbach, D., et al. 2007, ApJ, 671, L165
- Kalas, P., et al. 2008, Science 322, 1345
- Liseau, R., et al. 2010, this volume
- Matthews et al. 2010, this volume
- Pilbratt, G., et al. 2010, this volume
- Poglitsch, A., et al. 2010, this volume
- Stapelfeldt, K.R., et al. 2004, ApJS 154, 458

Stern, S.A. 1996, A&A 310, 999
 Su, K.Y.L., Rieke, G.H., Stansberry, J.A. et al. 2006, ApJ 653, 675
 Trilling et al. 2008, ApJ 674, 1086
 Wyatt, M.C., et al. 1999, ApJ 527, 918

¹ Dpt. Física Teórica, Facultad de Ciencias, Universidad Autónoma de Madrid, Cantoblanco, 28049 Madrid, Spain
 e-mail: carlos.eiroa@uam.es
² Max-Planck Institut für Astronomie, Königstuhl 17, 69117 Heidelberg, Germany
³ John Hopkins University, Dept. of Physics and Astronomy, 3701 San Martin drive, Baltimore, MD 21210, USA
⁴ INSA at ESAC, E-28691 Villanueva de la Cañada, Madrid, Spain
⁵ ESA Space Environment and Effects Section, ESTEC, PO Box 299, 2200 AG Noordwijk, The Netherlands
⁶ ESA Astrophysics & Fundamental Physics Missions Division, ESTEC/SRE-SA, Keplerlaan 1, NL-2201 AZ Noordwijk, The Netherlands
⁷ Université Joseph Fourier/CNRS, Laboratoire d'Astrophysique de Grenoble, UMR 5571, Grenoble, France
⁸ ESA-ESAC Gaia SOC. P.O. Box 78 E-28691 Villanueva de la Cañada, Madrid, Spain
⁹ LAEX, Centro de Astrobiología (INTA-CSIC), LAEFF Campus, European Space Astronomy Center (ESAC), P.O.Box 78, E-28691 Villanueva de la Cañada, Madrid, Spain
¹⁰ NASA Herschel Science Center, California Institute of Technology, 1200 E. California Blvd., Pasadena, CA 91125, USA
¹¹ Jet Propulsion Laboratory, California Institute of Technology, Pasadena, CA 91109, USA
¹² Onsala Space Observatory, Chalmers University of Technology, S-439 92 Onsala, Sweden
¹³ European Space Observatory, Alonso de Cordova 3107, Vitacura Casilla 19001, Santiago 19, Chile
¹⁴ Institut d'Astrophysique et de Géophysique, Université de Liège, 17 Allée du Six Août, B-4000 Sart Tilman, Belgium
¹⁵ NASA ExoPlanet Science Institute California Inst. of Technology, 1200 E. California Blvd., Pasadena, CA 91125, USA
¹⁶ NASA Goddard Space Flight Center, Exoplanets and Stellar Astrophysics, Code 667, Greenbelt, MD 20771, USA
¹⁷ UNINOVA-CA3, Campus da Caparica, Quinta da Torre, Monte de Caparica, 2825-149 Caparica, Portugal
¹⁸ Nagoya University, Japan.
¹⁹ Max-Planck-Institut für Kernphysik, Saupfercheckweg 1, D-69117 Heidelberg, Germany
²⁰ Kapteyn Astronomical Institute, Postbus 800, 9700 AV Groningen, The Netherlands
²¹ Astrophysikalisches Institut und Universitätssternwarte, Friedrich-Schiller-Universität, Schillergäßchen 2-3, 07745 Jena, Germany
²² Herschel Science Center, ESAC/ESA, P.O. BOX 78, 28691 Villanueva de la Cañada, Madrid, Spain
²³ Department of Physics and Astrophysics, Open University, Walton Hall, Milton Keynes MK7 6AA, UK
²⁴ Universidad Complutense de Madrid, Facultad de Ciencias Físicas, Dpt. Astrofísica, av. Complutense s/n. 28040 Madrid, Spain
²⁵ Observatoire de la Côte d'Azur, Boulevard de l'Observatoire, B.P. 4229, 06304 Nice Cedex 4, France
²⁶ Institute of Space and Astronautical Science (ISAS), Japan Aerospace Exploration Agency (JAXA), 3-1-1, Yoshinodai, Sagamihara, Kanagawa, 229-8510, Japan
²⁷ Department of Astronomy, Stockholm University, AlbaNova University Center, Roslagstullsbacken 21, SE-106 91 Stockholm, Sweden
²⁸ Institut de Ciències de l'Espai (CSIC-IEEC), Campus UAB, Facultat de Ciències, Torre C5, parell, 2a pl., E-08193 Bellaterra, Barcelona, Spain
²⁹ LESIA, Observatoire de Paris, 92195 Meudon France
³⁰ Rutherford Appleton Laboratory, Chilton OX11 0QX, UK
³¹ Christian-Albrechts-Universität zu Kiel, Institut für Theoretische Physik und Astrophysik, Leibnizstr. 15, 24098 Kiel, Germany